



Formation dynamics of mesocrystals composed of organically modified CeO₂ nanoparticles: Analogy to particle formation model

Journal:	<i>CrystEngComm</i>
Manuscript ID	CE-ART-03-2019-000473.R1
Article Type:	Paper
Date Submitted by the Author:	14-May-2019
Complete List of Authors:	<p>Litwinowicz, Andrzej-Alexander; Tohoku University Graduate School of Engineering School of Engineering Takami, Seiichi; Nagoya University Asahina, Shunsuke; JEOL Ltd., SM Business Unit; Tohoku University, IMRAM Hao, Xiaodong; Tohoku University Graduate School of Engineering School of Engineering Yoko, Akira; WPI – Advanced Institute for Materials Research (WPI-AIMR) Tohoku University Seong, Gimyeong; Tohoku Daigaku, A New Industry Creation Hatchery Center tomai, Takaaki; Tohoku University, Institute of Multidisciplinary Research for Advanced Materials Adschiri, Tadafumi; Tohoku Daigaku, New Industry Creation Hatchery Center; Tohoku University, Wpi AIMR; Tohoku Daigaku, Institute of Multidisciplinary Research for Advance Materials</p>

Formation dynamics of mesocrystals composed of organically modified CeO₂ nanoparticles: Analogy to particle formation model

Andrzej-Alexander Litwinowicz^{*a}, Seiichi Takami^{*b}, Shunsuke Asahina^c, Xiaodong Hao^a, Akira Yoko^d, Gimyeong Seong^e, Takaaki Tomai^f, and Tadafumi Adschiri^{*d,e,f}

a Graduate School of Engineering, Tohoku University, 6-6 Aramaki Aza-Aoba, Aoba-ku, Sendai 980 – 8579, Japan

b Department of Materials Process Engineering, Graduate School of Engineering, Nagoya University, Furo-cho, Chikusa-ku, Nagoya, 464-8603

c JEOL Ltd., 3-1-2 Musashino, Akishima, Tokyo 196-8558, Japan

d WPI – Advanced Institute for Materials Research (WPI-AIMR), Tohoku University, 2-1-1 Katahira, Aoba-ku, Sendai 980-8577, Japan

e New Industry Creation Hatchery Center, Tohoku University, 6-6-10, Aoba, Aramaki, Aoba-ku, Sendai 980-8577, Japan

f Institute of Multidisciplinary Research for Advanced Materials, Tohoku University, 2-1-1 Katahira, Aoba-ku, Sendai 980-8577, Japan

ABSTRACT

Mesocrystals, non-classical crystalline nanostructured materials composed of aligned nanoparticles, represent considerable potential for use in various engineering fields. Nevertheless, their formation mechanism and methods for size and morphology control remain unclear. For this study, the mesocrystal formation process in hydrothermal conditions was first observed for L-glutamic-acid-modified cerium oxide nanoparticle clusters using a flow reactor system able to control the reaction time to within 1 s. At reaction times of less than 1 s under 548 K, spherical agglomerations composed of truncated octahedral nanoparticles with random orientation were observed. Such spherical agglomerations altered their shape to cubic assemblies with an ordered superstructure as the reaction time proceeded to 8.0 s. Observations made using HRTEM and cross-section SEM with EBSD confirmed evolution from spherical polycrystal to cubic mesocrystal. The mesocrystal formation process was analogous to conventional crystal formation and growth, where primary nanoparticles act as monomers to form an ordered structure via non-ordered agglomeration. Based on the idea that organically modified nanoparticles behave similarly to monomers in conventional crystallization, mesocrystal size control was achieved by varying the primary nanoparticle concentration and the affinity of the solvent to the nanoparticles.

Keywords: Cerium oxide; Continuous hydrothermal synthesis; Mesocrystal; Nanoparticle

INTRODUCTION

Mesocrystals are nanocrystals aligned into ordered superstructures, with the assembled nanoparticles having the same orientation leading to a diffraction pattern similar to that of single crystals^{1,2}. The ordered structure is expected to exploit direction-dependent properties of nanocrystals such as ion mobility, electron mobility, and magnetism. High surface area and high porosity can be combined with benefits of single crystals using highly crystalline nanoparticles³. Moreover, obtaining heterointerfaces using different nanocrystals might be a subject for future development. Consequently, mesocrystalline materials are promising candidates for various applications such as photocatalysts⁴⁻⁵, lithium ion batteries⁶⁻⁷, biomedical applications⁸⁻⁹, and optical/electronic/magnetic applications including metamaterials. In spite of their marked potential, mesocrystals are not yet applied in industrial applications because efficient production processes of precisely controlled mesocrystals are still under development. Understanding their formation mechanisms and controlling the mesocrystal size and shape are crucially important to adjust their properties and to facilitate their use in diverse applications.

Hydrothermal technology presents suitable techniques for nanoparticle efficient production¹⁰. Small nanoparticles with a narrow size distribution are obtainable via continuous flow hydrothermal synthesis¹¹. Moreover, *in situ* organic surface modifications¹² of those nanoparticles are possible because of the characteristic phase behavior of high-temperature water, which makes a homogeneous phase with various organic molecules. Control of interactions between particles is enabled by surface modification¹³. Furthermore, it is possible to synthesize mesocrystals using hydrothermal techniques. Synthesis of highly orientated cubic nanoassembly of ceria has been demonstrated using a continuous flow hydrothermal synthesis in

the presence of modifiers such as dicarboxylic acids: hexanedioic acid^{14,15} and L-glutamic acid¹⁶. This method facilitates the precise size control of highly crystalline metal and metal oxide primary particles^{17,18} and also the mesocrystal shape and size^{19,20,21}. In the flow-type hydrothermal method, the metal salt precursor at room temperature is mixed with preheated water in a continuous reactor²². The reaction time can be adjusted simply by the reactor length. Consequently, snapshots of the crystal at different reaction times are obtainable to elucidate the mesocrystal formation mechanisms under hydrothermal conditions, which is not possible when using a batch reactor²³. Effectiveness of the flow-type system for analyzing crystallization was proved through synthesis of nanoparticles while controlling the particle size and shape by changing the pressure²⁴, temperature²⁵, mixing regime²⁶, and added surfactants²⁷.

The hierarchical structure, such as the mesocrystal structure formed by particles, is difficult to control because the structural formation mechanism of the secondary structure from nanoparticles has not been elucidated. Regarding the example of the secondary structure formation from nanoparticles, nanoparticle aggregation behavior during thin film coating under drying has been studied for the structural formation from particles²⁸. Nanoparticles can be regarded as building blocks of structural formation. Elucidating similarity and dissimilarity to atoms or molecule is expected to elucidate the mesocrystal formation mechanism. Consequently, in this study, the mesocrystal formation is investigated based on the analogy of particle formation.

To clarify the mesocrystal formation process in hydrothermal conditions, a flow-type hydrothermal system, with reaction time controlled precisely to accuracy of 1 s was used. Time-resolved experiments on the order of seconds are conducted to examine the mesocrystal formation process. The formation mechanism is studied by comparing ordinary crystallization of

nanocrystals. The mesocrystal particle size control can be demonstrated based on the formation mechanism.

EXPERIMENTAL SECTION

Cerium(III) nitrate hexahydrate, ethanol, and L-glutamic acid were purchased from Wako Pure Chemical Industries Ltd. Purified water was purchased from Yamato Kagaku Co. Ltd.

A flow reactor was used to synthesize organically modified cerium oxide. An illustration of the process is displayed as Schema 1. A cerium nitrate ($\text{Ce}(\text{NO}_3)_3$) solution with concentration of 0.01 mol L^{-1} was prepared as a precursor. As a capping agent for the formed nanocrystals, L-glutamic acid was dissolved into the provided cerium nitrate solution. The L-glutamic acid concentration was 0.03 mol L^{-1} (a molar ratio of cerium ion to surfactant of 1:3). The precursor was pumped into a reactor with a flow rate of 4 mL min^{-1} through an SUS 316 tube with 1.8 mm inner diameter using a high-pressure pump (PU-2080; Jasco Corp.) and mixed with preheated water at a T-shaped mixer (2.3 mm inner diameter). The preheated water was prepared by pumping purified water with a flow rate of 16 mL min^{-1} through a separate tube where it is heated in a furnace. The temperature was measured with thermocouples before and after the mixing point. After mixing, the solution passed an isothermal zone with the adjusted reaction temperature (fluid temperature was measured directly after the mixing point). The stream is then cooled quickly to room temperature with a water jacket and is passed through a $0.5 \mu\text{m}$ filter (Protective Filter SS-4TF-05; Swagelok Co.). The reaction time, which was defined as the time the flow requires from the mixing point to the cooler entrance, was varied by altering the length of the isothermal zone keeping flow rates at constant. Using this system, the reaction time can be controlled within accuracy of 1 s. The 25 MPa operating pressure was regulated using a

backpressure regulator (26-1700 Series; Tescom Corp.). In the case of reaction with ethanol, ethanol was added to the deionized water setting a molar fraction of ethanol after mixing with the precursor as 8%.

The crude nanoparticle dispersion was collected after the release in a glass flask and was filtrated under vacuum with a filter (VSWP09025, 0.025 μm pore size; Nihon Millipore Ltd.). After the filter cake was washed three times with 400 mL of purified water, the filter cake was dispersed in 75 mL of purified water and was freeze-dried for at least 24 hr.

To observe the particle size and morphology, transmission electron microscopy (TEM, H7650; Hitachi Ltd.) and scanning electron microscopy (SEM: JEOL JSM-7800) were used. High-resolution images and diffraction images were obtained using a field-emission transmission electron microscope (FE-TEM, JEM-2100F; JEOL). Cross-sectional SEM images and EBSD analyses were performed using SEM (JEOL, JSM-7800) equipped with an electron backscattered diffraction (EBSD) detector (Oxford). An argon ion beam was applied for cross-section polishing; details are published elsewhere¹⁵. Cross sections of the samples were prepared using a cross section polisher (JEOL, IB-09010). Details about the cross section preparation and analyses are presented elsewhere¹⁵. X-ray diffraction of the obtained freeze-dried sample was measured using a diffractometer (SmartLab 9MTP; Rigaku Corp.). The crystallite size was calculated based on the Halder-Wagner method with whole pattern fitting in the range of 20-80°. The XRD patterns and the Halder-Wagner plots are shown in *Supporting Information*. For analyses of the conversion of cerium precursor to solid products after the reaction, samples of the mother lye from the filtration were ultracentrifuged at 50,000 rpm for 1 hr. The supernatant from the centrifugation was used for inductively coupled plasma (ICP) measurements (iCAP 6500; Thermo Fisher Scientific Inc.).

RESULTS

Figure 1 and Figure 2 respectively present HRTEM images of cerium oxide clusters synthesized in 0.7 s and 8.0 s in the presence of L-glutamic acid under 0.01 M concentration and with a molar ratio of [Ce] to [Glu] of 1:3 at 548 K. As shown in Figure 1, spherical clusters of ca. 72 nm were synthesized at a reaction time of approximately 0.7 s. As shown in Figure 2, cubic-like clusters of 104 nm were obtained at approx. 8.0 s. High-resolution figures (Figures 1c,d; Figures 2c,d) show that clusters of both types comprise ca. 20 nm primary truncated octahedral particles with large {111} surface and small {100} surface exposed. The diffraction pattern for the spherical cluster (Figure 1b) shows a polycrystal structure, implying that the primary particles did not align with the same orientation. However, the diffraction pattern of the cubic-like clusters gives a crystalline structure resembling that of a single crystal (Figure 2b) indicating highly orientated primary particles. These results affirm that the final product is a cubic mesocrystal consisting of CeO₂ nanoparticles.

Structural change of the cluster indicates rearrangement of truncated octahedral primary building blocks from spherical polycrystal to a cubic mesocrystal in less than 8.0 s. In an earlier SEM study¹⁵, it was observed that cubic nanoassemblies of ceria are composed by edge-sharing of primary octahedral particles with an exposed {111} facet. In this study, similar edge sharing structures exist as shown in Figure 3. A reasonable mechanism for the formation from polycrystal to mesocrystal is the grain rotation-attachment mechanism to reduce the surface energy of primary modified particles in the polycrystal resulting from misorientation. Grain rotation is the rotation of neighboring grains to reduce the misorientation angles and to share the same crystallographic orientation³²⁻³³, which can engender mesocrystal,³⁴ as observed in the present case.

SEM images of CeO₂ synthesized in a range of 0.7–8.0 s are shown in Figure 4. Figure 5 shows the corresponding cluster sizes analyzed by TEM together with the crystallite size of primary CeO₂ particles evaluated by XRD patterns with Halder-Wagner method. Initially, the spherical cluster of ca. 72 nm at approx. 0.7 s, first shrinks to approx. 42 nm as the residence time increases to approx. 2.0 s, with subsequent growth of particles to 104 nm associated with shape alteration to a cubic structure. Differences in product structure were found with the changing residence time, suggesting that mesocrystal formation definitely occurred in hydrothermal conditions. This cluster shrinkage is expected to derive from the rearrangement of primary particles, as discussed later. In contrast to the cluster size differences with reaction time, the crystallite size remains nearly constant around 20 nm, which is similar to the primary particle sizes observed using FE-TEM. The estimated conversion of cerium measured using ICP analyses at residence times of 0.7, 2.0, 3.7, and 8.0 s are, respectively, 19, 36, 45, and 75%. Consequently, the formation of new primary particles occurs with progressive residence time. It is aligned with the existing cubic cluster causing cluster growth.

The crystallographic orientation of the primary nanocrystals inside the obtained nanoclusters was studied to confirm the formation process. The cross-section SEM analyses were conducted with electron backscatter diffraction (EBSD) analyses for the polycrystal and the mesocrystal to reconfirm the formation process. Cross-sectional SEM images with a crystallographic orientation map are displayed in Figure 6. In the spherical clusters shown in Figure 6 a and b, hollow structures were observed, implying that loose agglomeration occurred by the van der Waals attraction force of the primary particle. The crystal orientation of the spherical cluster detected using EBSD supports the diffraction pattern of the HRTEM analyses showing that a polycrystal was formed. In contrast, SEM images of the cubic cluster (Figure 6 d and e) show no hollow

structure. This diminishment of the hollow in the clusters by rearrangement of the primary particles is expected to be the reason that the cluster showed shrinkage associated with shape alteration from spherical to cubic. Moreover, EBSD mapping indicates the same orientation of the primary particle, reconfirming the mesocrystal evolution. The structural change of the cluster reflects the rearrangement of truncated octahedral primary building blocks from spherical polycrystal to cubic mesocrystal in less than 8.0 s.

DISCUSSION

Here, the mesocrystal formation mechanism is discussed based on analogy to ordinary particle formation. As shown in Schema 2, in the case of ordinary crystalline particle formation, nucleation occurs from atomic or molecular scale monomers, followed by crystal growth with monomer diffusion to the crystal surface. In the case of the mesocrystal formation, the difference is in the monomers. Agglomeration of primary nanoparticles formed in hydrothermal condition occurs, followed by orientation of primary nanoparticles and mesocrystal growth with primary particle diffusion. Consequently, the agglomeration step can be regarded as nucleation from primary particles; the orientation and growth resemble the crystal growth in ordinary particle formation. Results demonstrated that the dispersion behavior of organic modified nanoparticles in organic solvents can be predicted^{36,37}, considering organically modified nanoparticles as quasi-molecules. In other words, the primary particle dispersion can be described by the "solubility" of the particle in a solvent as molecules. In the case of the mesocrystal formation, the primary particle surface is covered with glutamic acid, which has a hydrophilic nature. Although it is hydrophilic, the acidic carboxylic group is more stable on the basic surface of CeO₂ than in bulk water. Surface modification of the primary particles, followed by bridging particles, occurred. The clustering driving force in the case of mesocrystal formation is the interaction between

organic molecules and nanoparticles in addition to the van der Waals forces between nanoparticles and the surface energy³⁰. Whether mesocrystal forms or not is dependent on the combinations of solvents, modifiers, and particles.

Alternation of the initial concentrations of the reactant and of the "solubility" under reaction conditions were conducted to observe phase separation behavior, i.e., phase separation of particles from metal salt solution (nanocrystal) or that of clusters from particle dispersion (mesocrystal). To change the solubility, ethanol was introduced as the antisolvent³⁸ to the preheated water stream before mixing with the precursor. Unmodified CeO₂ nanoparticles were also synthesized from cerium nitrate under 548 K, 25 MPa, and 0.7 s for comparison. Figures 7 a and c portray TEM images of the products obtained with 0.01 M and 0.005 M of cerium in precursor solutions. The particles were smaller with lower precursor concentrations and the addition of ethanol (8 mol%), as shown in Figure 7 e. However, in the case of mesocrystal formation from L-glutamic acid modified nanoparticles, the mesocrystal size change shows similar behavior to that described above for conventional crystallization from molecules. The cluster size also decreased with the decrease in the precursor concentration (Figure 7 d) and with addition of the antisolvent (Figure 7, f), compared to the reference condition (Figure 7 b). It is noteworthy that the crystallite sizes estimated from the XRD patterns of the particle with the lower concentration and the addition of ethanol were, respectively, 16.4 nm and 14.4 nm. Those crystallite sizes are similar to the crystallite size (17.8 nm) of the cluster obtained at high concentration without ethanol. Therefore, the dominant factor for cluster size is not the primary particle size, but the clustering behavior of the primary particles.

For both nanocrystal formation and mesocrystal formation, the particle size (nanocrystal) and cluster size (mesocrystal) decreased with decreased concentration or addition of ethanol.

Regarding the classical nucleation theory, a decrease in the monomer concentration engenders formation of larger particles because of the decrease in the degree of supersaturation. It might be readily apparent that this tendency differs from that observed for concentration dependence in this study. A possible model to explain the results from the precursor concentration dependence is collisional growth or coalescence^{39, 40}, which dominated the increases in both nanocrystal and mesocrystal size, as shown in Schema 3. In the case of ethanol addition, coalescence was suppressed, but the frequency of the collisional growth is expected to be the same. The interfacial energy between particles and solvents would be decreased by ethanol addition. The interfacial energy determines the adhesion force between particles, thus the weakened interfacial energy suppresses the coalescence during the collision process resulting in the smaller final particle size (nanocrystal) and cluster size (mesocrystal). It can be understood that the organically modified primary particles behave similarly to monomers in a conventional crystallization manner. Based on an analogical manner to nanocrystal formation, the mesocrystal size is controllable in the hydrothermal system.

The determinant factor of particle size by the collisional growth is diffusivity of particles. Order estimation of the diffusivity time constant (L^2/D [s]) was conducted with a diffusion constant (D), particle size, and a distance between particles (L) using the Stokes–Einstein equation. For the 20-nm particles, rapid diffusion on the order of 10^{-4} s occurs. In contrast, slower diffusion of the order of 10^{-1} s is obtained for 100-nm particles. These results confirmed that the collisional growth of the primary particles is reasonable for the second order reaction and that collision of larger particles occurs only slightly during the reaction. The kinetics of the primary particle collision determines the final cluster particle size of the mesocrystal (approx. 100-nm particles).

Another interesting point from the analogy of crystal growth is the crystallinity of the products. At the initial stage of the mesocrystal formation, sphere aggregation occurred from primary particles. The sphere aggregation which formed was further aligned by grain rotation to share the same facet³⁵, leading to cluster size reduction. Apparently, stabilization occurs by rearrangement of the primary particles. During hydrothermal synthesis, crystallinity of nanoparticles generally improves along with the increase in reaction time. The morphological changes of the mesocrystals observed in this study can be interpreted as analogy of improved crystallinity in the nanocrystal formation.

CONCLUSION

The formation process of organically modified cerium oxide mesocrystal from a spherical cluster was observed using a flow-type reactor under hydrothermal conditions in the presence of L-glutamic acid. First, in hydrothermal conditions with L-glutamic acid, organically modified CeO₂ nanoparticles were formed. With increasing reaction time, the primary nanoparticles in the loose agglomeration order themselves to form a cubic CeO₂ mesocrystal by sharing the same faces to reduce the surface energy. Subsequently, mesocrystal size growth occurred because of the alignment of the non-agglomerated primary particle and newly formed primary particle with increased residence time. The observed formation of agglomeration and the mesocrystal evolution suggest that primary organically modified nanoparticles behave as a monomer for conventional crystallization. This finding is expected to facilitate the synthesis of crystalline mesocrystals with size control in an environmentally friendly scalable continuous hydrothermal process applying single-crystal formation and growth models. Moreover, the continuous hydrothermal synthesis system supports the investigation of the mesocrystal formation

mechanism under hydrothermal conditions of second order. Detailed analyses of the general formation of mesocrystals can be conducted using this system.

AUTHOR INFORMATION

Corresponding Author

*E-mail: andrzej@litwinowicz.com

*E-mail: takami.seiichi@material.nagoya-u.ac.jp

*E-mail: tadafumi.ajiri.bi@tohoku.ac.jp

ACKNOWLEDGMENTS

This study is supported by the grants from the Japan Society for the Promotion of Science (JSPS); KAKENHI (Grant Number, JP16H06367), the New Energy and Industrial Technology Development Organization (NEDO), JST MIRAI (Grant Number JPMJMI17E4) JST CREST (JPMJCR16P3), Japan, and WPI – Advanced Institute for Materials Research (WPI-AIMR), Tohoku University established by World Premier International Research Center Initiative (WPI), Ministry of Education, Culture, Sports, Science and Technology (MEXT), Japan.

REFERENCES

1. H. Colfen and M. Antonietti, *Angew Chem Int Ed Engl*, 2005, 44, 5576-5591.

2. J. J. De Yoreo, P. U. Gilbert, N. A. Sommerdijk, R. L. Penn, S. Whitlam, D. Joester, H. Zhang, J. D. Rimer, A. Navrotsky, J. F. Banfield, A. F. Wallace, F. M. Michel, F. C. Meldrum, H. Colfen and P. M. Dove, *Science*, 2015, 349, aaa6760.
3. L. Zhou and P. O'Brien, *J Phys Chem Lett*, 2012, 3, 620-628.
4. A. Y. Zhang, L. L. Long, W. W. Li, W. K. Wang and H. Q. Yu, *Chem Commun*, 2013, 49, 6075-6077.
5. B. Hu, L. H. Wu, S. J. Liu, H. B. Yao, H. Y. Shi, G. P. Li and S. H. Yu, *Chem Commun*, 2010, 46, 2277-2279.
6. S. Chen, M. Wang, J. F. Ye, J. G. Cai, Y. R. Ma, H. H. Zhou and L. M. Qi, *Nano Research*, 2013, 6, 243-252.
7. J. Ye, W. Liu, J. Cai, S. Chen, X. Zhao, H. Zhou and L. Qi, *Journal of the American Chemical Society*, 2011, 133, 933-940.
8. T. Lee and C. W. Zhang, *Pharm Res*, 2008, 25, 1563-1571.
9. S. L. Zhong, Y. Lu, M. R. Gao, S. J. Liu, J. Peng, L. C. Zhang and S. H. Yu, *Chemistry*, 2012, 18, 5222-5231.
10. M. Yoshimura and K. Byrappa, *Journal of Materials Science*, 2008, 43, 2085-2103.
11. T. Adschiri, K. Kanazawa and K. Arai, *Journal of the American Ceramic Society*, 1992, 75, 1019-1022.
12. J. Zhang, S. Ohara, M. Umetsu, T. Naka, Y. Hatakeyama and T. Adschiri, *Advanced Materials*, 2007, 19, 203-+.

13. T. Arita, J. Yoo and T. Adschiri, *Journal of Nanoparticle Research*, 2010, 12, 2567-2578.
14. S. Takami, S. Ohara, T. Adschiri, Y. Wakayama and T. Chikyow, *Dalton transactions*, 2008, DOI: 10.1039/b801099d, 5442-5446.
15. S. Asahina, S. Takami, T. Otsuka, T. Adschiri and O. Terasaki, *Chemcatchem*, 2011, 3, 1038-1044.
16. A. A. Litwinowicz, S. Takami, D. Hojo, N. Aoki and T. Adschiri, *Chemistry Letters*, 2014, 43, 1343-1345.
17. K. Byrappa and T. Adschiri, *Progress in Crystal Growth and Characterization of Materials*, 2007, 53, 117-166.
18. T. Adschiri, *Chemistry Letters*, 2007, 36, 1188-1193.
19. V. Singh, T. Naka, S. Takami, A. Sahraneshin, T. Togashi, N. Aoki, D. Hojo, T. Arita and T. Adschiri, *Dalton transactions*, 2013, 42, 16176-16184.
20. K. He, B. Song, L. T. Zhan, W. W. Lu, J. Li, G. L. Zhao and G. R. Han, *Crystengcomm*, 2016, 18, 754-758.
21. Y. J. Geng, G. Lian, J. Wang, H. B. Si, Q. L. Wang, D. L. Cui and C. P. Wong, *Crystal Growth & Design*, 2016, 16, 2466-2471.
22. J. A. Darr, J. Zhang, N. M. Makwana and X. Weng, *Chemical reviews*, 2017, 117, 11125-11238.
23. E. V. Sturm Nee Rosseeva and H. Colfen, *Chemical Society reviews*, 2016, 45, 5821-5833.

24. I. Gonzalo-Juan, B. Ferrari, M. T. Colomer, M. A. Rodriguez, A. J. Sanchez-Herencia, P. Y. Koh and A. S. Teja, *Materials Chemistry and Physics*, 2012, 134, 451-458.
25. K. Shibuki, M. Takesue, T. M. Aida, M. Watanabe, H. Hayashi and R. L. Smith, *The Journal of Supercritical Fluids*, 2010, 54, 266-271.
26. N. Aoki, A. Sato, H. Sasaki, A. A. Litwinowicz, G. Seong, T. Aida, D. Hojo, S. Takami and T. Adschiri, *J Supercrit Fluid*, 2016, 110, 161-166.
27. S. Kubota, T. Morioka, M. Takesue, H. Hayashi, M. Watanabe and R. L. Smith, *J Supercrit Fluid*, 2014, 86, 33-40.
28. N. Kobayashi, S. Sakai, Y. Sasaki, M. Kubo, T. Tsukada, K. Sugioka, S. Takami and T. Adschiri, *Journal of Chemical Engineering of Japan*, 2018, 51, 460-468.
29. T. Togashi, T. Naka, S. Asahina, K. Sato, S. Takami and T. Adschiri, *Dalton transactions*, 2011, 40, 1073-1078.
30. Z. L. Wang and X. D. Feng, *J Phys Chem B*, 2003, 107, 13563-13566.
31. S. V. Kuchibhatla, A. S. Karakoti and S. Seal, *Nanotechnology*, 2007, 18, 075303.
32. D. Moldovan, D. Wolf and S. R. Phillpot, *Acta Materialia*, 2001, 49, 3521-3532.
33. D. Moldovan, V. Yamakov, D. Wolf and S. R. Phillpot, *Phys Rev Lett*, 2002, 89, 206101.
34. J. Fang, B. Ding and H. Gleiter, *Chemical Society reviews*, 2011, 40, 5347-5360.
35. H. Norenberg and J. H. Harding, *Surface Science*, 2001, 477, 17-24.

36. T. Arita, Y. Ueda, K. Minami, T. Naka and T. Adschiri, *Industrial & Engineering Chemistry Research*, 2010, 49, 1947-1952.
37. T. Arita, J. Yoo and T. Adschiri, *J Phys Chem C*, 2011, 115, 3899-3909.
38. A. Cabañas, J. Li, P. Blood, T. Chudoba, W. Lojkowski, M. Poliakoff and E. Lester, *The Journal of Supercritical Fluids*, 2007, 40, 284-292.
39. C. J. Denis, C. J. Tighe, R. I. Gruar, N. M. Makwana and J. A. Darr, *Crystal Growth & Design*, 2015, 15, 4256-4265.
40. F. D. Wang, V. N. Richards, S. P. Shields and W. E. Buhro, *Chemistry of Materials*, 2014, 26, 5-21.

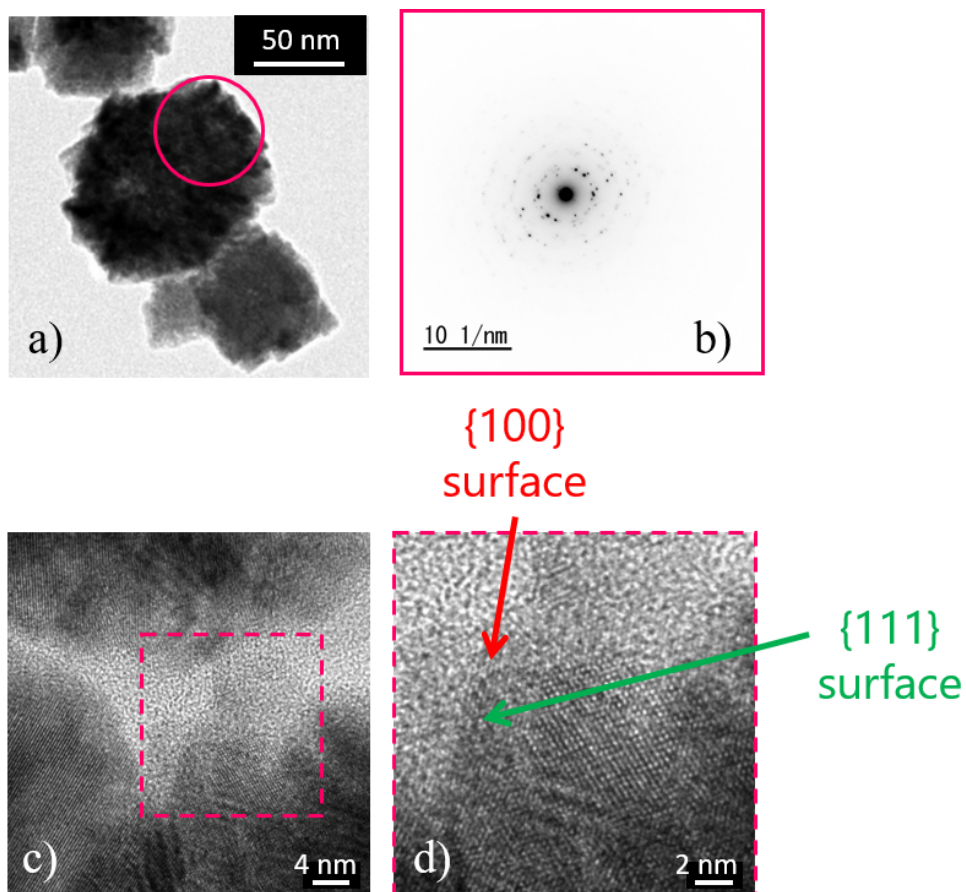
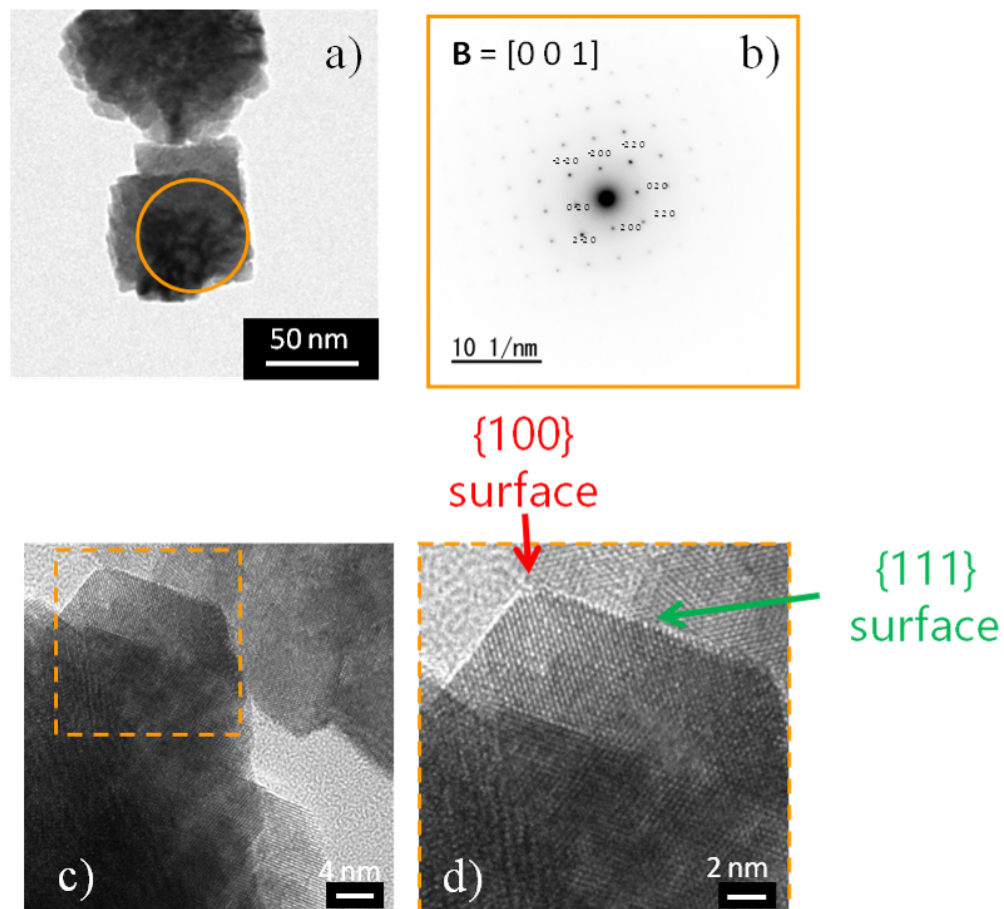


Figure 1 HRTEM sample of the spherical CeO₂ cluster: a) low magnification (pink circle represents the area of the diffraction analyses), b) diffraction pattern, c) higher resolution image, and d) magnified image of c) to analyze the primary particle shape (reaction conditions 548 K, 25 MPa, 0.7 s, [Ce]:[Glu] 1:3).

138x124mm (150 x 150 DPI)



135x122mm (150 x 150 DPI)

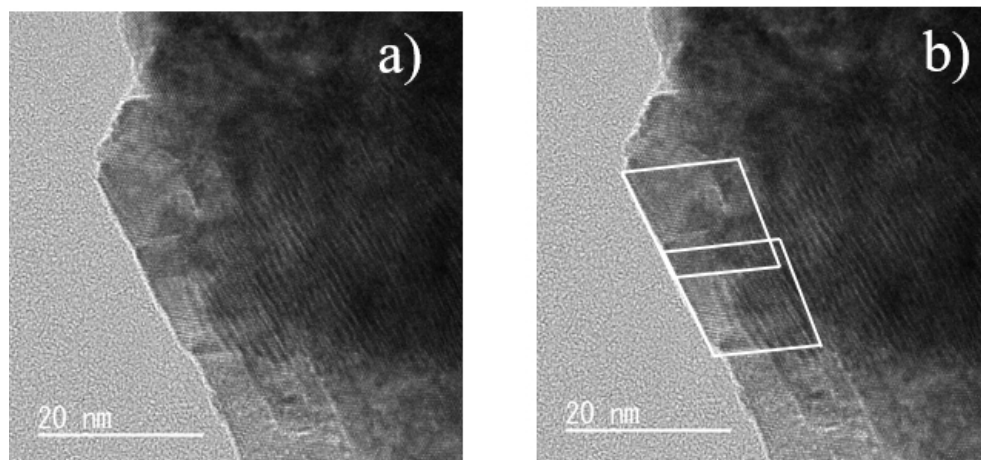


Figure 3 a) Highly magnified HTREM image of cubic ceria and b) illustration of the truncated octahedral primary particle of b for easier identification (reaction conditions: 548 K, 25 MPa, 8.0 s, [Ce]:[Glu] 1:3).

110x51mm (150 x 150 DPI)

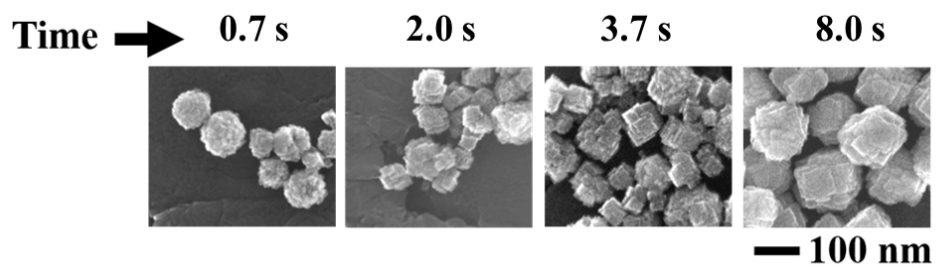


Figure 4 SEM images showing shape alteration depending on the reaction time synthesized at 548 K and 25 MPa.

170x51mm (150 x 150 DPI)

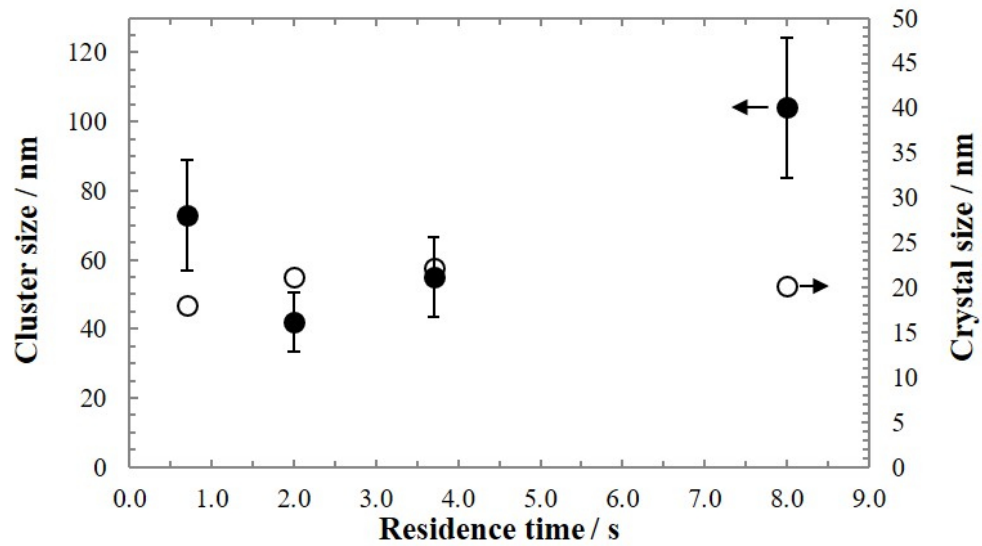


Figure 5 Time dependence of cluster size evaluated by TEM and crystal size estimated using the XRD pattern via Halder-Wagner method: filled; cluster size (left axis), open; crystal size (right axis).

131x73mm (150 x 150 DPI)

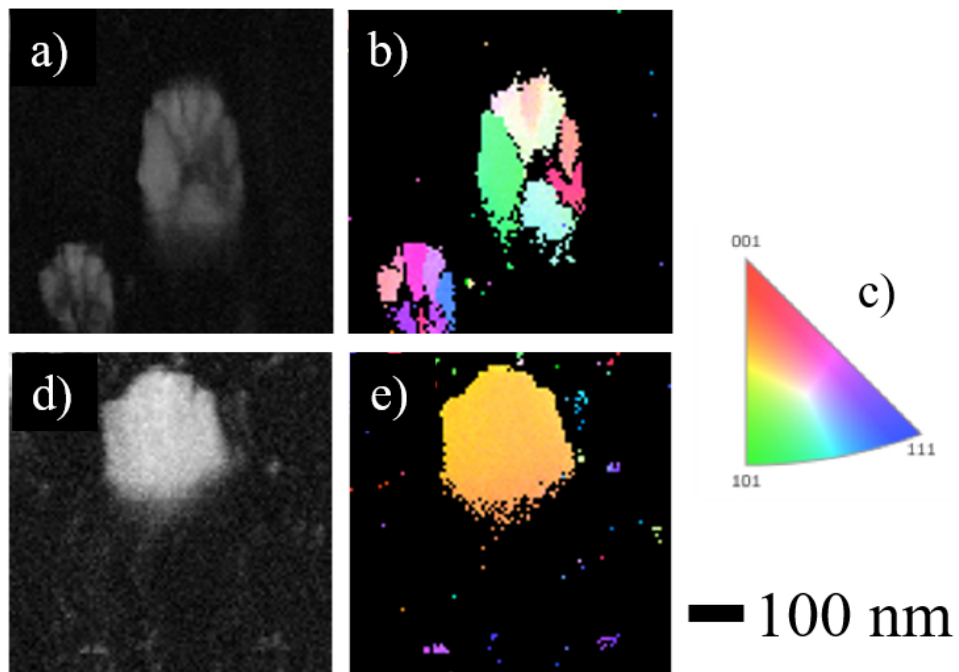


Figure 6. a) Cross-sectional and b) EBSD image of spherical cluster (548 K, 25 MPa, 0.7 s, [Ce]:[Glu] 1:3). c) Spectra map of the crystal orientation. d) Cross-sectional and e) EBSD image of cubic cluster (548 K, 25 MPa, 8.0 s, [Ce]:[Glu] 1:3)

128x88mm (150 x 150 DPI)

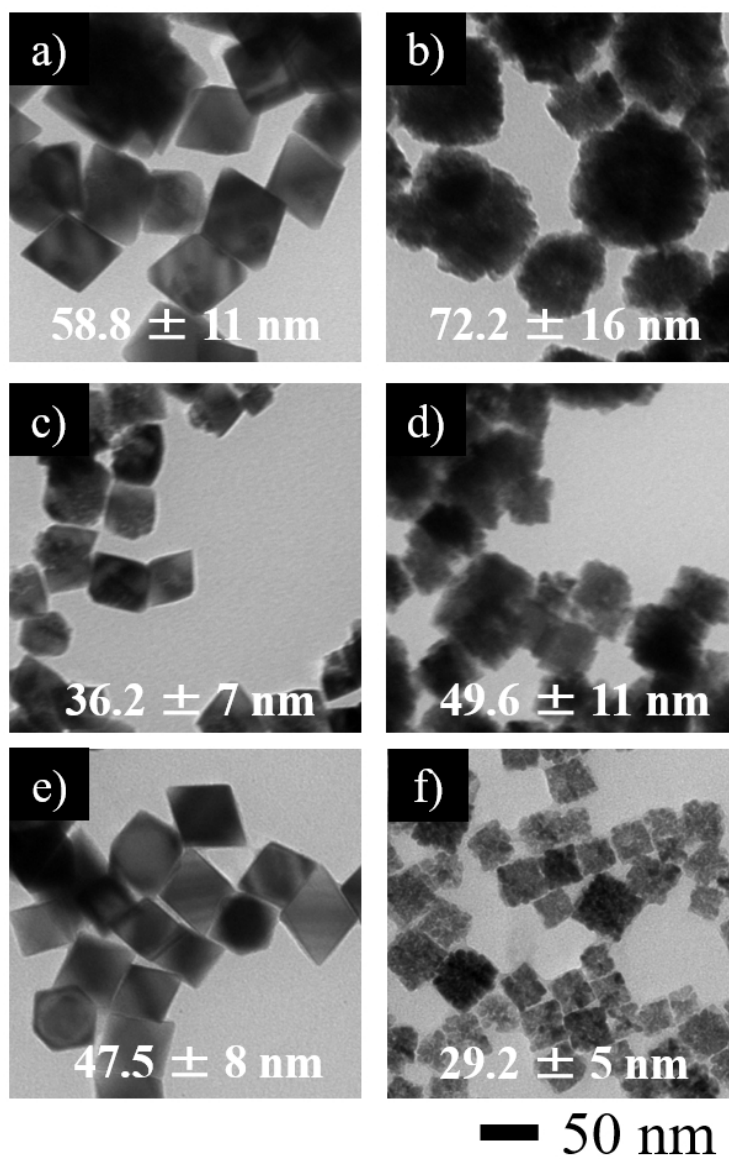


Figure 7. CeO₂ synthesized in the absence of Glu (Reaction condition: 548 K, 25 MPa, 0.7 s) a) [Ce] 0.01M, c) [Ce] 0.005M, e) [Ce] 0.01M and xEthanol = 0.08. CeO₂ synthesized in the presence of Glu (Reaction condition: 548 K, 25 MPa, 0.7 s, [Ce]:[Glu] 1:3) b) [Ce] 0.01M, d) [Ce] 0.005M, f) [Ce] 0.01M and xEthanol = 0.08. The numbers at the bottom of each TEM image represent the average size analyzed from of at least 100 particles.

103x164mm (150 x 150 DPI)